Supplementary material to "A unified theory of slender wings in asymmetric motion":

RANS simulations of steady flow about a slender swept wing

Gil Iosilevskii[1]

Faculty of Aerospace Engineering, Technion, Haifa 32000, Israel

Ilya Kislitsin[2]

Israeli Computational Fluid Dynamics Center, Caesarea Industrial Park 30889, Israel

Outline

This supplementary presents a few numerical simulations of aerodynamic loads on a slender wing and compares them with the theory of the companion paper. The simulations were based both on the vortex lattice method described in Appendix H of the companion paper, and on solution or Reynolds-averaged Navier-Stokes (RANS) equations. Notation in this file conforms that of the companion paper. All quantities are reduced using the semi-span of the aft segment s_0, the fluid velocity v and the fluid density ρ as the respective units. The units of force and moment are $\rho v^2 s_0^2$ and $\rho v^2 s_0^3$ respectively.

The model wing

The test model for RANS simulations is shown in figure S1. It was based on a 1125 by 50 by 6 mm extrusion with a NACA0012 profile. Forward and aft corners (situated on the sharp edge of the profile) were trimmed. The forward cut was rounded with half the local thickness as the local radius. The aft cut was sharpened. When set at 10 degrees relative to the flow direction ($\lambda = 0.175$), it had $s_0 = 25.4$ mm, and, consequently, $x_n = -5.19$ and $x_t = 38.45$. These numbers slightly changed with a sweep angle. Details are furnished in table S1 below. Test model for potential flow simulations is described in Appendix H of the companion paper. It had

[1] Email: igil@technion.ac.il
[2] Email: ilya@iscfdc.com

fixed $x_n = -5$ and $x_t = 39$, and it had zero thickness.

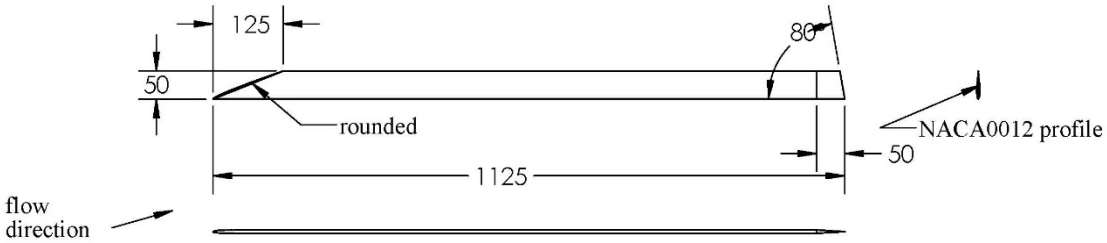

Figure S1: Three views of the model wing for RANS simulations. Dimensions are in mm.

RANS simulations

The global (primed) reference frame (see the companion paper) was affixed to the body, with its *y*-axis connecting the leading edge (the lower edge on figure S1) with the trailing edge at the corner between forward and aft segments, and *x*-axis in the plane of the wing, aligned with the flow direction when set with no angle of attack (figure S2). Except for a shift along the *y*-axis, local and global coordinate systems coincide. All moments were referred to the origin of the reference frame, at the end of the forward segment (figure S2).

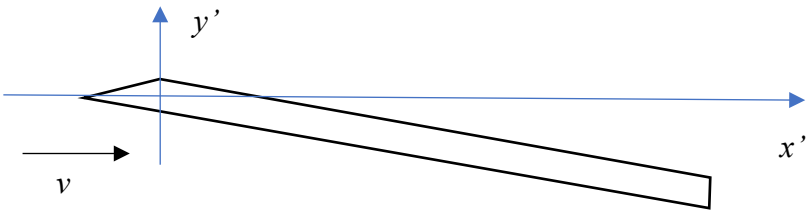

Figure S2: The reference frame. Except for the shift along the *y*-axis, the global (primed) and local (unprimed) frames coincide. The origin of the global system is located at the middle of the after-most section of the forward segment.

The fluid was assumed to have the properties of standard air. The flow velocity was invariably 60 m/s. It yielded the body-length-based Reynolds number of approximately 400,000. Two overlapping grids were generated (figure S3): a global grid extending 40 m along the *x*-axis, and 20 m along the other two, and the body grid with 18M cells. The cell size near

the body was 5 microns, less than one tenth of the estimated viscous length scale of 100 microns. The solver was EZAir from Israeli CFD center. The turbulence model was *k*-*ω*. No slip boundary condition was imposed on the surface of the body and free stream condition on the outer boundaries. Angle of attack and, to the same end, different sweep angles, were generated by imposing different far-field free-stream conditions. Simulated cases are summarized in table S1.

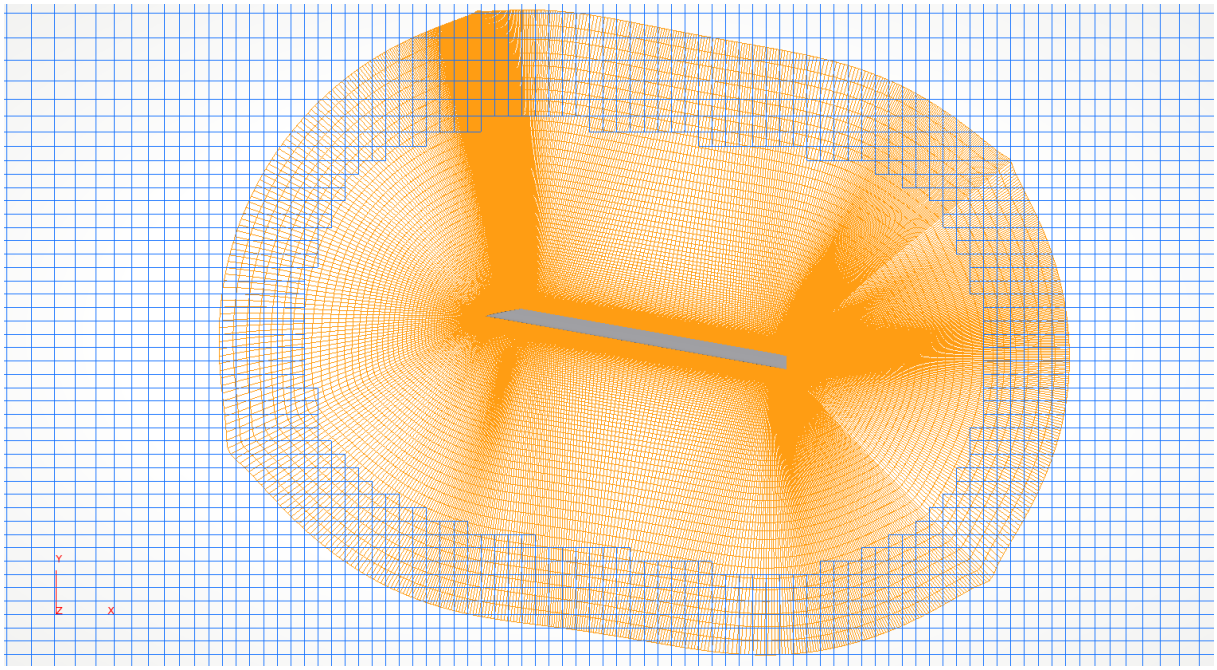

Figure S3: An extract of the computational domain. It comprised two grids in an overset configuration.

Table S1: Simulated cases and results

case	λ	α	x_n	x_t	$F_{x'}$	$F_{y'}$	$F_{z'}$	$M_{y'}$
1	0.1745	0	-5.19	38.45	0.3583	0.01160	-0.0009	0.0187
2	0.1745	0.01	-5.19	38.45	0.3561	0.00042	0.3133	5.7231
3	0.1745	0.05	-5.19	38.45	0.3039	-0.25360	1.5873	28.350
4	0.1695	0.01	-5.19	38.5	0.3545	-0.00175	0.3046	5.5390
5	0.1645	0.01	-5.19	38.6	0.3530	-0.00388	0.2954	5.3496
6	0.1245	0.01	-5.17	39.1	0.3401	-0.02010	0.2238	3.8604
7	0.0745	0.01	-5.12	39.6	0.3210	-0.03795	0.1410	2.1370

Simulation results are shown by red pentagrams in figure S4. *Z*-component of the force and its center of pressure (defined as $x_{cp} = -M_{y'}/F_{z'}$) are shown 'as is'; *x*- and *y*-components

of the force are shown as differences between the simulated force at angle of attack and the simulated reference at zero angle of attack (this is case 1 in table S1). Since zero-angle of attack reference was simulated only at one sweep angle, only two points for *x*- and *y*- components could be added to the figure (these are cases 2 and 3).

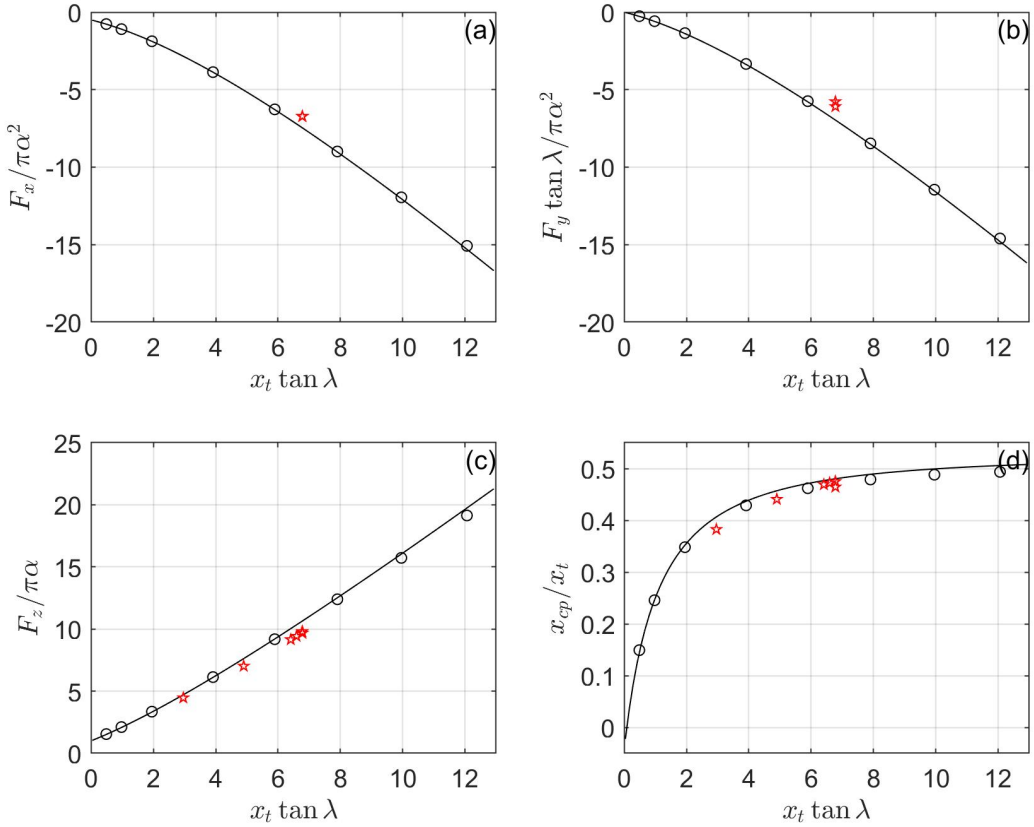

Figure S4: *x*-, *y*- and *z*- components of the pressure loads acting on the wing, and well as their center of pressure as functions of λ. Pentagrams represent RANS simulations; circles represent potential flow simulations; lines represent equations (S.5)-(S.10).

Potential flow simulations

Potential flow simulations were based on the vortex lattice method. Details can be found in Appendix H in the companion paper. As mentioned already, the test model had $x_n = -5$ and $x_t = 39$. Wing's motion was set by equation (S.1) with $\alpha = 0.01$. θ was zero. Computational grid had 21 chord-wise and 21 span-wise divisions. Simulations continued for 10 time steps,

each 10 units long (as in case 2 of the companion paper). Simulation results are shown by circles in figure S4.

Theoretical predictions

It was assumed that $\theta(t,x)=0$; the angle of attack was generated by plunging the wing downward, along the negative *z*-axis, with (reduced) velocity $\alpha = v_z$:

$$z_0(t,x) = -\alpha t \mathrm{H}(t). \tag{S.1}$$

Under these circumstances,

$$w_1(t,x) = 0 \tag{S.2}$$

by equation (3.7) in the companion paper, whereas

$$w_0(t,x) = w_{3/4}(t,x) = \alpha \tag{S.3}$$

by equations (3.6) and (5.24). Consequently,

$$W_{3/4}(\infty,x,\tan\lambda) = \alpha\tan\lambda\int_0^x \Psi_0(x'\tan\lambda)\,dx' = \alpha\,\Psi_1(x\tan\lambda) \tag{S.4}$$

by (5.48), (5.42) and (5.43), and

$$F_x(\infty) = -\frac{\pi}{2}a^2 - 2\pi\tan\lambda\int_0^{x_t} W_{3/4}^2(\infty,x,\tan\lambda)\,dx = -\pi\alpha^2\left(\frac{1}{2}+2\int_0^{x_t\tan\lambda}\Psi_1^2(x)\,dx\right), \tag{S.5}$$

$$F_{y'}(\infty) = -2\pi\int_0^{x_t} W_{3/4}^2(\infty,x,\tan\lambda)\,dx = -2\pi\alpha^2\cot\lambda\int_0^{x_t\tan\lambda}\Psi_1^2(x)\,dx, \tag{S.6}$$

$$F_{z'}(\infty) = \pi\alpha + 2\pi\tan\lambda\int_0^{x_t} W_{3/4}(\infty,x,\tan\lambda)\,dx = \pi\alpha\left(1+2\Psi_2\left(x_t\tan\lambda\right)\right), \tag{S.7}$$

$$M_{y'}(\infty) = \pi\alpha\int_{x_n}^0 s^2(x)\,dx - 2\pi\tan\lambda\int_0^{x_t} W_{3/4}(\infty,x,\tan\lambda)\,x\,dx + \dots$$

$$= \pi\alpha\int_{x_n}^0 s^2(x)\,dx - 2\pi\alpha x_t\left(\Psi_2\left(x_t\tan\lambda\right) - \frac{\Psi_3\left(x_t\tan\lambda\right)}{x_t\tan\lambda}\right) + \dots \tag{S.8}$$

by (6.2), (6.3), (6.4) and (6.10). The last two equations here recover equations (7.29) and (7.30)

in the companion paper; the difference between the first two and the respective equations (7.27) and (7.28) is in a different orientation of the reference frame. With a triangular forward segment,

$$\int_{x_n}^{0} s^2(x)\,dx = -\frac{1}{3}x_n\,. \tag{S.9}$$

The center of pressure is located at

$$x_{cp} = -M_{y'}(\infty)\big/F_{z'}(\infty)\,; \tag{S.10}$$

because both $F_{z'}(\infty)$ and $M_{y'}(\infty)$ are proportional to α, it coincides with the aerodynamic center. Equations (S.5)-(S.10) are represented by solid lines in figure S4. $x_n = -5$ and $x_t = 39$ were substituted where needed, as in potential flow simulations.